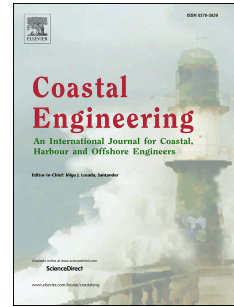


Journal Pre-proof

Hydrodynamic investigation on an OWC wave energy converter integrated into an OWT monopile

Yu Zhou, Dezhi Ning, Wei Shi, Lars Johanning, Dongfang Liang



PII: S0378-3839(20)30001-6

DOI: <https://doi.org/10.1016/j.coastaleng.2020.103731>

Reference: CENG 103731

To appear in: *Coastal Engineering*

Received Date: 2 January 2020

Revised Date: 1 May 2020

Accepted Date: 26 May 2020

Please cite this article as: Zhou, Y., Ning, D., Shi, W., Johanning, L., Liang, D., Hydrodynamic investigation on an OWC wave energy converter integrated into an OWT monopile, *Coastal Engineering* (2020), doi: <https://doi.org/10.1016/j.coastaleng.2020.103731>.

This is a PDF file of an article that has undergone enhancements after acceptance, such as the addition of a cover page and metadata, and formatting for readability, but it is not yet the definitive version of record. This version will undergo additional copyediting, typesetting and review before it is published in its final form, but we are providing this version to give early visibility of the article. Please note that, during the production process, errors may be discovered which could affect the content, and all legal disclaimers that apply to the journal pertain.

© 2020 Published by Elsevier B.V.

Credit Author Statement

Yu Zhou: Conceptualization, Methodology, Software, Validation, Investigation, Writing Original Draft.

Dezhi Ning: Conceptualization, Resources, Supervision, Writing-Reviewing and Editing.

Wei Shi: Writing-Reviewing and Editing.

Lars Johanning: Writing-Reviewing and Editing.

Dongfang Liang: Writing-Reviewing and Editing.

Journal Pre-proof

Hydrodynamic investigation on an OWC wave energy converter integrated into an OWT monopile

Yu Zhou¹, Dezhi Ning^{1*}, Wei Shi¹, Lars Johanning^{1,2}, Dongfang Liang^{1,3}

¹State Key Laboratory of Coastal and Offshore Engineering, Dalian University of Technology, Dalian,
116024, China

² College of Engineering, Mathematics and Physical Sciences, University of Exeter, Penryn Campus,
Penryn, Cornwall TR10 9FE, UK.

³. Department of Engineering, University of Cambridge, Cambridge, CB2 1PZ, UK

Abstract

Multi-functional platform is a promising way to enhance the economic power production from multiple renewable energy sources. This paper investigates numerically and experimentally the hydrodynamic performance of an oscillating water column (OWC) wave energy converter (WEC), integrated into a monopile-mounted offshore wind turbine (OWT). Based on linear potential flow theory, a 3D time-domain numerical model was developed, based on the higher-order boundary element method, to investigate the coupled hydrodynamic response of a cylindrical-type OWC device. A nonlinear pneumatic model was utilized to simulate the turbine damping. Experiments on the integrated system were carried out in a wave flume at Dalian University of Technology. The numerical results agree well with the experimental studies, including i) the surface elevation and air pressure inside the chamber, ii) wave pressure on the OWT monopile and iii) hydrodynamic efficiency. Furthermore, the effects of the OWC damping and wave steepness on the OWC-OWT system were investigated. It was found that the introduction of the OWC can significantly reduce the horizontal force and overturning moment on the OWT monopile, and that the wave steepness has a significant influence on the OWC efficiency, especially at resonance.

Keywords: Oscillating Water Column; OWT Monopile; Wave loads; HOBEM; Physical

* Corresponding author. Email address: dzning@dlut.edu.cn

Nomenclature

Notation

| | |
|-----------------------|---|
| A | Incident wave amplitude |
| b_w | Thickness of the chamber wall |
| B | Width of the flume |
| d | Draft of the OWC chamber wall |
| d_c | Air chamber height |
| $D=2R_2$ | External diameter of the OWC chamber |
| D_o | Turbine diameter |
| F | Wave force |
| g | Gravitational acceleration |
| G | Green function |
| h | Water depth |
| k | Incident wave number |
| M | Wave moment |
| $n = (n_x, n_y, n_z)$ | Normal vector |
| $\overline{N_w}$ | Average peak values of chamber surface-elevation, air pressure and efficiency |
| p | Point pressure |
| p_s | Source point |
| P_{air} | Air pressure |
| ΔP | Amplitude of the point pressure |
| ΔP_{air} | Amplitude of the air pressure |
| P_{owc} | Extracted wave power |
| P_{inc} | Averaged incident wave energy |
| q_f | Field point |
| Q | Air volume flux |
| r_0 | Inside radii of the damping layer |
| r_1 | Outside radii of the damping layer |
| $1/R_0$ | Rankine source |
| R_1 | Radius of the OWT monopile |
| $1/R_z$ | Image of Rankine source about the seabed |
| S | Boundary surface |
| S_B | Mean wet body surface |
| S_D | Seabed |
| S_f | Chamber cross-sectional area |
| S_{IF} | Chamber free surface |
| S_{OF} | Free surface outside the chamber |
| t | Time |

| | |
|-----------------------|--|
| T | Incident wave period |
| u | Air flow velocity through the turbine orifice |
| $u_c(t)$ | Normal vertical velocity of chamber free surface |
| (x_0, y_0, z_0) | Rotational center coordinates |
| z | Vertical coordinate |
| ω | Angular frequency |
| ρ | Water density |
| ϕ | Spatial potential |
| ϕ_i | Incident potential |
| ϕ_s | Scattered potential |
| η_s | Scattered wave elevation around the OWC |
| η_{crest} | Crest amplitude of the free surface |
| λ | Wave length |
| μ_1 | Artificial damping coefficient |
| μ_2 | Nonlinear pneumatic damping coefficient |
| $\nu_{(r)}$ | Damping coefficient of the damping layer |
| α | Solid angle coefficient |
| ε | Opening ratio |
| $\bar{\sigma}$ | Relative error |
| $\partial/\partial n$ | Normal derivative on the solid surface |
| ξ | Hydrodynamic efficiency |

28

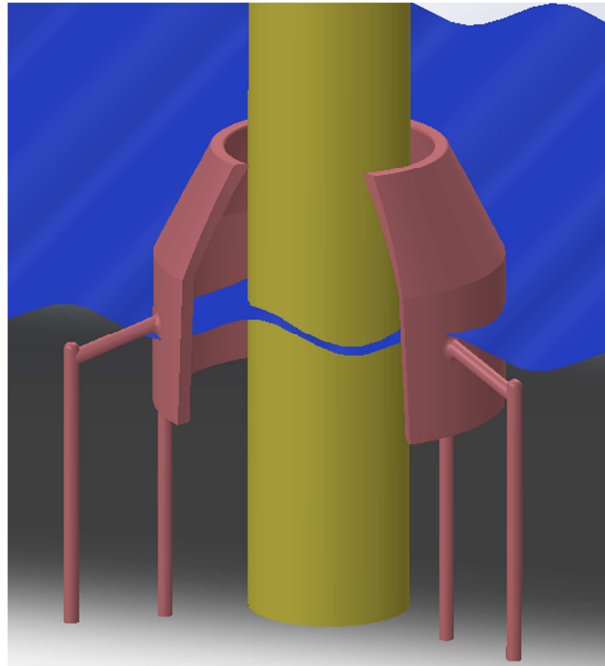
29 **1. Introduction**

30 Offshore renewable energy is one of the most promising sources to address the climate
31 change and the shortage of fossil fuels (Pechak et al., 2011). Various ocean energy are under
32 consideration, including offshore wind, wave, tide range, marine currents and salinity
33 gradients etc (Bahaj, 2011). Offshore wind turbine (OWT) technologies have seen a
34 significant acceleration around the world, with the sector installing a record of 6.1GW in 2019
35 (Ohlenforst and Council, 2019). A large number of monopile offshore wind turbines have
36 been constructed in the relatively shallow waters with depth smaller than 30 m (Achmus et al.,
37 2009). By the end of 2018, monopiles remain the most popular foundation type, representing
38 81.9% of all installed foundations in Europe (Wind-Europe, 2019). As an offshore structure,
39 the OWT monopiles are subject to not only aerodynamic loads from wind but also to
40 hydrodynamic loads from wave and currents (Paulsen et al., 2019). Frequently re-occurring
41 large wave loads can induce fatigue damage and lateral deformation of the structure elements

42 and ground foundation (Slot et al., 2019). Hence, the OWT monopiles present one of the main
43 design challenges related to the reliable operation and survivability (Wu et al., 2019).
44 Conversely, wave energy also represents a potential energy resource with a higher power
45 density than wind power (Sheng, 2019). The oscillating water column (OWC) wave energy
46 converter (WEC) is a promising technology due to its simplicity and reliability (Heath, 2012;
47 Falcão and Henriques, 2016). However, compared with solar and wind power devices,
48 commercial exploitation of the OWC WECs is still limited as a source of electrical power
49 device (Aemesto et al., 2014).

50 Combining the wind and wave energy converters together could be beneficial for utilizing
51 the space and enhance energy extraction (Wan et al., 2015). It would also be beneficial for the
52 wind and wave energy converters to share the infrastructures such as foundations, piles,
53 power substations and cables etc to reduce the investment (Ren et al., 2018). In recent years, a
54 lot of research have been carried out regarding the combined exploitation of the wave and
55 offshore wind energy (Pérez-Collazo et al., 2015; Cheng et al., 2019). Sarmiento et al. (2019)
56 performed an experimental study on a floating semi-submersible platform integrated with
57 three OWC WECs under various wind, wave and current conditions. Michailides et al. (2016)
58 carried out a physical model test to study the properties of a semi-submersible wind turbine
59 combined with flap-type WECs. Haji et al. (2018) proposed a symbiotic design, including a
60 standalone floating wind turbine and an OWC array, which has the potential to reduce the cost
61 by 14% and increase the power production by 9%. Liang et al. (2017) investigated the
62 hydrodynamic performance of a floating offshore floating renewable energy system, which
63 integrates three types of renewable energy converters (wind, wave & current). The multiple
64 system was found to reduce the dynamic response and increase the overall power production.
65 Perez-Collazo et al. (2018) tested the hydrodynamic response of a hybrid wind-wave systems
66 in an experimental campaign. Perez-Collazo et al. (2019) proved the feasibility of attaching an
67 OWC device to the offshore fixed wind substructure. Following Perez-Collazo`s concept, this
68 paper proposes an updated design of the integrated system. Fig. 1 shows the concept of the
69 OWC device integrated into a fixed OWT monopile. A cylindrical chamber is placed around

70 the OWT monopile to enable the OWC integration.



71
72 Fig. 1 Concept of the OWC device integrated into a fixed OWT monopile

73

74 The OWC device integrated into a floating supporter is another innovative design for
75 capturing the wave energy from deep sea. A large number of researches have been conducted
76 worldwide. Falcão et al. (2014) optimized and designed an axisymmetric Spar-buoy OWC
77 device and the turbine damping system. A biradial impulse turbine was proved to be a better
78 performance for the energy conversion. Gomes et al. (2016) simulated a heaving Spar-buoy
79 OWC device to evaluate the effects of the side walls on the hydrodynamics of the device in a
80 wave channel. Further, an experiment of floating Spar-buoy devices was also carried out for
81 large-scale exploitation of the offshore renewable energy (da Fonseca et al., 2016). It was
82 found that the array configuration performs a better performance than the isolated device. He
83 et al. (2017) carried out a physical experiment to investigate the hydrodynamics of a dual
84 pneumatic chambers OWC device installed on floating breakwaters. Elhanafi et al. (2017)
85 investigated a 3D offshore OWC device subject to different wave amplitude and lip
86 submergence. However, the motion of the floating device can counteract the OWC capability
87 for capturing the wave energy. Compared with the floating device, the OWC integration into
88 fixed offshore structures, such as breakwaters and OWT monopile, can perform higher

89 efficiency and reliability due to motionless structure.

90 A number of models have been developed to design and optimize the OWC converters
91 (Mahnamfar and Altunkaynak, 2017; Simonetti et al., 2017). The analytical method was
92 applied for the preliminary design of the OWC devices (Ning et al., 2018). Zheng et al. (2018)
93 investigated the interaction between a hybrid wave farm and the wave field by means of a
94 semi-analytical model. Based on linear potential flow theory, He et al. (2019) developed an
95 analytical model to study the hydrodynamics of a pile-supported OWC breakwater. Zheng et
96 al. (2019) evaluated the effects of the array layout on the performance of the OWC devices
97 based on an analytical solution. However, the analytical method can only be possible in
98 special configurations, and it fails to capture the viscous loss and vortex shedding (Rezanejad
99 et al., 2013). A large number of viscous-flow models based on the N-S equations have been
100 developed to optimize the geometric parameters of the OWC devices (Elhanafi et al., 2017). A
101 3D CFD model has been constructed to investigate the impacts of power take-off (PTO)
102 damping on the behaviour of a fixed Multi-Chamber OWC device (Shalby et al., 2019) and
103 good agreement between numerical and experimental results was observed. Based on the
104 RANS equations and the volume of fluid (VOF) method, Xu et al. (2016) considered a
105 quadratic pressure loss coefficient to simulate a cylindrical OWC device in a wave flume.
106 They found that the quadratic coefficient varies slightly with the wave period and wave height.
107 However, viscous-flow models require a lot of computer resources (Chen et al., 2019). Based
108 on the potential-flow theory, the higher-order boundary element method (HOBEM) has been
109 applied to the OWC device (Koo and Kim, 2010). Wang et al. (2018) applied a time-domain
110 HOBEM to simulate the nonlinear and viscous influences on a fixed OWC device, facilitated
111 by experiments. Ning et al. (2019) carried out a fully nonlinear numerical simulation to
112 cross-check the experimental results of a land-based dual-chamber OWC device.

113 This paper carries out numerical and experimental investigations on an OWC wave
114 energy converter integrated into a fixed OWT monopile. It aims to simulate the hydrodynamic
115 performance of the OWC device and the wave loads on the OWT monopile to prove the
116 feasibility of the coupled OWC and OWT system. Section 2 presents the experimental model

117 and the HOBEM model. The nonlinear pneumatic damping is introduced to represent the
118 turbine. In section 3, the effects of the PTO damping and wave steepness on the
119 hydrodynamics of the integrated system are discussed. Finally, the conclusions of this study
120 are summarized in Section 4.

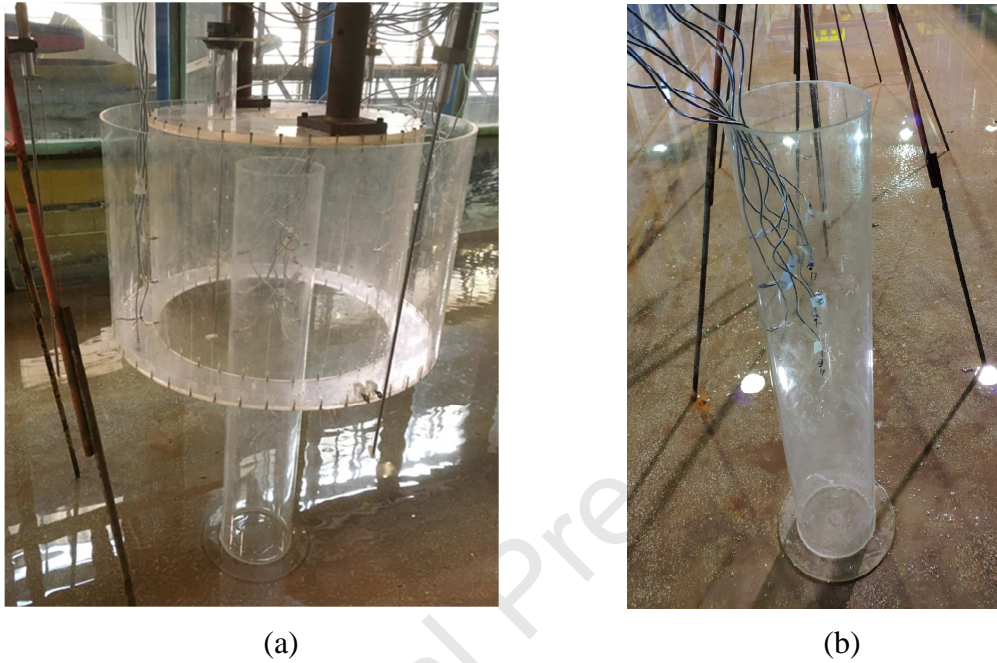
121

122 2. Experimental and numerical models

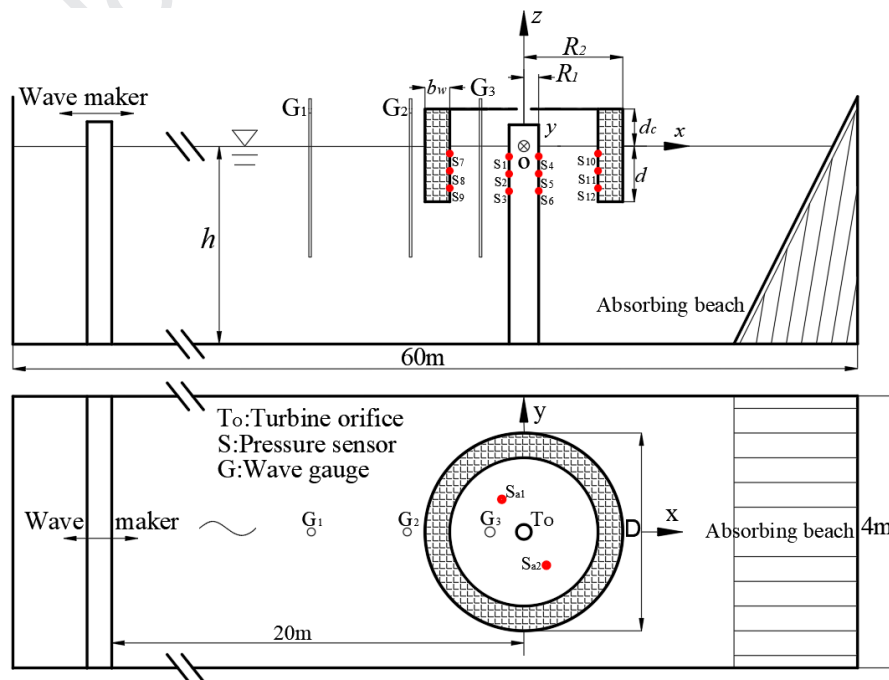
123 2.1. Experiment setup

124 A physical 3D model of the OWC integrated system, as shown in Fig. 2(a), was studied
125 at a 1:20 scale in a wave-current flume at the State Key Laboratory of Coastal and Offshore
126 Engineering in Dalian University of Technology. The flume is 60 m in length and 4 m in
127 width, with a maximum water depth of 2.5 m. The single OWT monopile, as shown in Fig.
128 2(b), was also investigated for the comparative purpose. The model to be investigated was
129 fixed at the center of the flume, as shown in Fig. 3. The water depth h was 1.0m in all cases. A
130 Cartesian coordinate system $Oxyz$ is defined with its origin at the center of the OWC. The
131 radius of the OWT monopile R_1 is 0.1 m, and the external diameter of the OWC chamber is D
132 $= 2R_2 = 0.8$ m. The effects of lateral flume walls can be ignored as discussed by Soares (1995)
133 since $B/D \geq 5$, where B is the width of the flume. The draft of the OWC chamber wall d is 0.3
134 m. The thickness of the chamber wall was fixed to be $b_w = 0.1$ m. The air chamber height, i.e.,
135 the distance between the static water surface and the chamber ceiling, was set to be $d_c = 0.2$ m.
136 In the scale-model experiment, the pneumatic air of the chamber can be considered ideal by
137 ignoring the thermodynamic effects (Medina-Lopez et al., 2016). In order to simulate the
138 effects of nonlinear turbine damping, a circular orifice, with a diameter $Do = 0.104$ m (Ning et
139 al., 2020), is introduced at the position $To (0m, 0m, 0.2m)$ as labelled in Fig. 3. The opening
140 ratio ε (i.e., the ratio between the orifice area and the area of the internal OWC chamber) is
141 3.38%. In the present study, three LG1 type wave gauges, i.e., G_1 – G_3 , as shown in Fig. 3,
142 were positioned to measure surface elevations along the centerline of the flume. Fig. 4(a)
143 shows the wave gauges and the DS30 type acquisition system. Two CY200 type pressure
144 sensors positioned at the top of the chamber, i.e. $S_{a1} (0.11m, -0.11m, 0.2m)$ and $S_{a2} (-0.11m,$
145 $0.11m, 0.2m)$, were used to record the air pressure at a sampling rate of 100 Hz. The 485-20

146 type acquisition system for the pressure sensors is shown in Fig. 4(b). In order to capture the
 147 pressure variations around the OWC system, twelve pressure sensors (S_1 - S_{12}) were placed
 148 around the OWT monopile and the OWC chamber wall, as shown in Fig. 3. The positions of
 149 the pressure sensors are listed in Table 1.



152 Fig. 2. Photographs of the experimental models (a) the OWC integrated system and (b) the OWT
 153 monopile.



156 Fig. 3. Experiment layout. Top: a side view showing the OWC device, the wave gauges and the
 157 pressure sensors. Bottom: a plan view of the orifices and the air pressure sensors.
 158



Fig. 4. The testing apparatus.

Table 1 Positions of the pressure sensors.

| | Position(m) | Position(m) | Position(m) | Position(m) | | | |
|----------------|-----------------|----------------|----------------|----------------|------------------|-----------------|-----------------|
| S ₁ | (-0.1, 0, -0.1) | S ₄ | (0.1, 0, -0.1) | S ₇ | (-0.3, 0, -0.07) | S ₁₀ | (0.3, 0, -0.07) |
| S ₂ | (-0.1, 0, -0.2) | S ₅ | (0.1, 0, -0.2) | S ₈ | (-0.3, 0, -0.17) | S ₁₁ | (0.3, 0, -0.17) |
| S ₃ | (-0.1, 0, -0.3) | S ₆ | (0.1, 0, -0.3) | S ₉ | (-0.3, 0, -0.27) | S ₁₂ | (0.3, 0, -0.27) |

Table 2 Wave conditions for the tank test.

| | | | | | | | | | | | | |
|---------------|------|------|------|------|------|------|------|------|------|------|------|------|
| kh | 3.33 | 2.81 | 2.6 | 2.42 | 2.26 | 2.11 | 1.99 | 1.87 | 1.68 | 1.53 | 1.2 | 1 |
| (mm) | 16.7 | 17.7 | 18.4 | 19.8 | 22.2 | 23.0 | 25.6 | 26.5 | 29.8 | 34.0 | 41.0 | 55.2 |
| A (mm) | — | — | 29.9 | — | 33.2 | 35.0 | 39.8 | — | — | — | — | — |
| ($kA=0.05$) | — | — | 38.6 | — | 44.3 | 46.0 | 54.8 | — | — | — | — | — |
| A (mm) | — | — | — | — | — | — | — | — | — | — | — | — |
| ($kA=0.10$) | — | — | — | — | — | — | — | — | — | — | — | — |

| | | | | | | | | | | | | |
|-----------|---|---|------|---|------|------|------|---|---|---|---|---|
| A(mm) | - | - | 55.7 | - | 66.2 | 71.2 | 78.4 | - | - | - | - | - |
| (kA=0.15) | | | | | | | | | | | | |

166

167 In the experiment, a series of monochromatic waves were generated in the wave-current
 168 flume to simulate the ocean waves, as listed in Table 2. The wave amplitude A varied with the
 169 wave number k , so as to obtain the desired wave steepness kA . In order to investigate the
 170 effect of the wave nonlinearity, four different wave steepness $kA = 0.05, 0.075, 0.10, 0.15$ were
 171 considered as shown in Table 2.

172 In this study, the hydrodynamic efficiency of the OWC device can be calculated as the
 173 ratio between the pneumatic power and the power of the corresponding incident wave (Ning
 174 et al., 2015). The wave power extracted by the OWC device (i.e., P_{owc}) can be calculated by
 175 the time-average integration of the product of the air volume flux Q and chamber air pressure
 176 P_{air} (Morris-Thomas et al., 2007) as follows:

$$177 \quad P_{owc} = \int_{S_f} \overline{P_{air}(t) \cdot Q(t)} dS = \frac{S_f}{T} \int_t^{t+T} P_{air}(t) \cdot u_c(t) dt, \quad (1)$$

178 where t denotes time, $u_c(t)$ is the normal vertical velocity of interior free surface. T denotes the
 179 period of the incident wave, S_f is the cross-sectional area of the free surface in the chamber.

180 The average energy flux per unit wave crest length P_{inc} is

$$181 \quad P_{inc} = \frac{\rho g A^2 \omega}{4k} \left(1 + \frac{2kh}{\sinh 2kh} \right), \quad (2)$$

182 where ρ is the water density, g the gravitational acceleration and ω is the angular frequency
 183 that can be determined according to the wave dispersion equation $\omega^2 = gk \tanh(kh)$.

184 Therefore, the hydrodynamic efficiency can be defined as:

$$185 \quad \xi = \frac{P_{owc}}{P_{inc} \cdot 2(R_2 - b_w)}, \quad (3)$$

186

187 2.2. Numerical model

188 Based on linear potential-flow theory, a 3D time-domain HOBEM was applied to
 189 investigate the hydrodynamic performance of the OWC integrated system. Fig. 5(a) shows the

190 numerical setup of the OWC integrated system. The system can be considered as a concentric
 191 cylindrical model. A Cartesian coordinate system $Oxyz$ is defined in the same way as in the
 192 experimental model shown in Fig. 3. It is assumed that the fluid is incompressible, inviscid
 193 and the motion is irrotational. The wave field around the device can be described by a
 194 complex spatial potential $\phi(x, y, z, t)$, which satisfies the Laplacian equation. Following the
 195 perturbation expansion procedure, the spatial potential ϕ can be divided into a known
 196 incident potential ϕ_i and an unknown scattered potential ϕ_s . The scattered potential ϕ_s
 197 satisfies the Laplacian equation:

$$198 \quad \nabla^2 \phi_s(x, y, z, t) = 0, \quad (4)$$

199 The scattered potential is subject to the impermeable condition at the bottom S_D and the solid
 200 body surface S_B :

$$201 \quad \frac{\partial \phi_s}{\partial n} = -\frac{\partial \phi_i}{\partial n}, \text{ on } S_D \text{ and } S_B \quad (5)$$

202 where $\partial/\partial n$ denotes the normal derivative on the solid surface. In order to analyze the wave
 203 motion in a finite domain, a sponge layer is introduced to absorb the reflected waves from the
 204 device (Ferrant, 1993), as shown in Fig. 5(b). To simulate the viscous loss and vortex
 205 shedding, a linear damping term is included on the free surface dynamic boundary condition
 206 inside the chamber (Kim, 2003). Following the Taylor expansion, the kinematic and dynamic
 207 boundary conditions on the free surfaces S_{IF} and S_{OF} can be expressed as (Ning et al., 2016):

$$208 \quad \begin{cases} \frac{\partial \eta_s}{\partial t} = \frac{\partial \phi_s}{\partial z} - v_{(r)} \eta_s \\ \frac{\partial \phi_s}{\partial t} = -g \eta_s - \frac{P_{air}}{\rho} - \mu_1 \frac{\partial \phi}{\partial n} - v_{(r)} \phi_s \end{cases}, \quad (6)$$

209 where η_s denotes the scattered wave elevation around the device, μ_1 is the artificial damping
 210 coefficient and $v_{(r)}$ is the damping coefficient of the damping layer. The second and third
 211 terms in the right-hand side of dynamic condition, represent the pneumatic pressure and the
 212 viscous effects induced by the OWC shell, respectively. These two terms are only considered
 213 inside the OWC chamber. The damping coefficient $v_{(r)}$ can be expressed as:

$$v_{(r)} = \begin{cases} \omega \left(\frac{r-r_0}{\lambda} \right)^2 & r_0 \leq r \leq r_1 = r_0 + \lambda \\ 0 & r < r_0 \end{cases}, \quad (7)$$

where λ is the wave length, r_0 and r_1 are the inside and outside radii of the damping layer respectively. The air pressure P_{air} can be linked to the square of the flow velocity (Sheng et al., 2013):

$$P_{air}(t) = \mu_2 |u(t)| u(t), \quad (8)$$

where u is the air flow velocity through the circular orifice, μ_2 is the nonlinear pneumatic damping coefficient which characterizes the turbine damping. Both μ_1 and μ_2 can be determined with the trial and error technique by matching the numerical predictions with the experimental measurements.

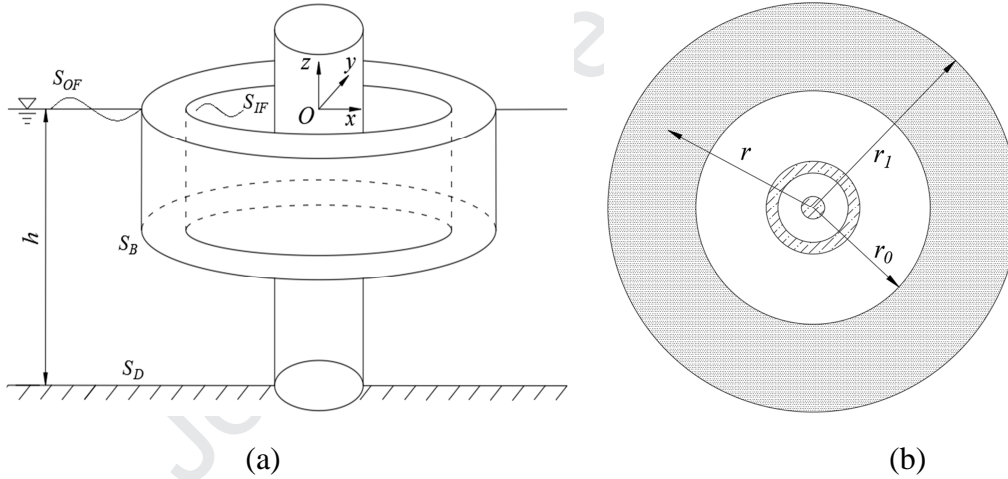


Fig. 5. Computational model: (a) the sketch of the OWC integrated model, (b) the illustration of the sponge layer.

The Green's second identity can be applied to the above boundary value problem with the Rankine source and its image about the seabed as the Green function (Bai and Teng, 2013).

$$G(p_s, q_f) = -\frac{1}{4\pi} \left(\frac{1}{R_0} + \frac{1}{R_z} \right), \quad (9)$$

where $p_s = (x_1, y_1, z_1)$ and $q_f = (x, y, z)$ are the source point and the field point, respectively, and

$$234 \quad \begin{cases} R_0 = \sqrt{(x-x_1)^2 + (y-y_1)^2 + (z-z_1)^2} \\ R_z = \sqrt{(x-x_1)^2 + (y-y_1)^2 + (z+z_1+2h)^2} \end{cases}, \quad (10)$$

235 Then, the integral equation for the scattered wave can be obtained:

$$236 \quad \alpha \phi_s(p_s) = \iint_S \left[\phi_s(q_f) \frac{\partial G(q_f, p_s)}{\partial n} - G(q_f, p_s) \frac{\partial \phi_s(q_f)}{\partial n} \right] dS, \quad (11)$$

237 where the boundary surface S includes the mean free surface (S_{OF} and S_{IF}) and the solid
 238 surface, α is the solid angle coefficient. A higher-order boundary element method is used to
 239 solve the boundary integral equation numerically. In the time domain, the simulation is
 240 advanced using the fourth-order Adams-Bashforth predictor-corrector method to predict the
 241 free surface and potential. The detailed procedure is referred to Jin et al. (2017). After solving
 242 Eq. (11), the spatial potential around the OWC integrated system can be obtained. According
 243 to following the Bernoulli equation, the pressure inside the OWC integrated system can also
 244 be obtained:

$$245 \quad p(t) = -\rho \frac{\partial \phi}{\partial t} + P_{air}(t), \quad (12)$$

246 The second term at the right side in Eq.(12) will be neglected if the single OWT monopile
 247 without OWC integration is considered.

248 The wave force and moment on the OWT monopile can be calculated by integrating the
 249 pressure over the wet surface of the inner cylinder:

$$250 \quad F = \iint_{S_{monopile}} p n dS, \quad (13)$$

$$251 \quad M = \iint_{S_{monopile}} p [(z-z_0)n_x - (x-x_0)n_z] dS, \quad (14)$$

252 in which $n = (n_x, n_y, n_z)$, $F = (F_x, F_y, F_z)$, (x_0, y_0, z_0) is the rotational center defined to be the
 253 monopile center at the seabed, i.e., (0 m, 0 m, -1 m). $S_{monopile}$ denotes the wet surface of the
 254 OWT monopile.

255

256 2.3. Model validation

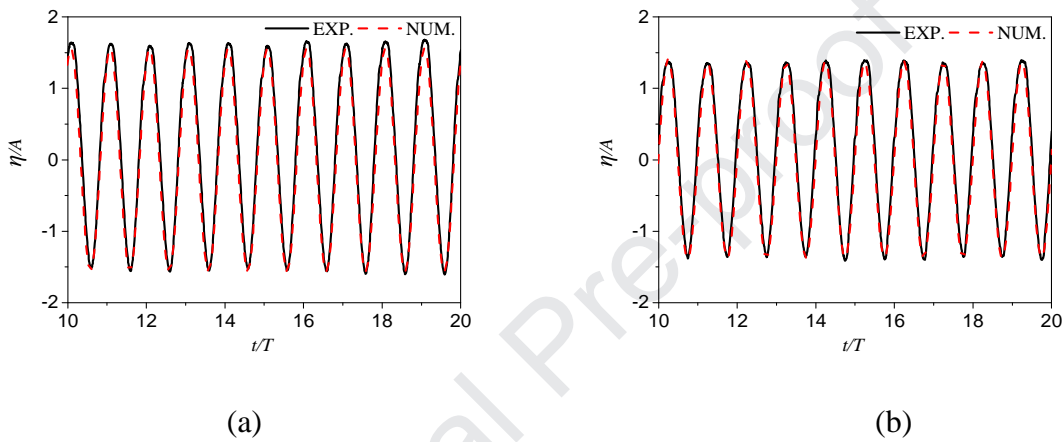
257 In the present study, the geometric parameters of the HOBEM model are the same as

258 those of the experimental model, as seen in figure 3. The outer and inner radii of the damping
 259 layer, as shown in Fig. 5(b), are set to be $r_1 = 2\lambda$ and $r_0 = \lambda$, respectively. The parameters of the
 260 incident waves are listed in Table 2. After convergent tests, the numbers of the computational
 261 elements on the free surfaces outside and inside the OWC chamber and monopile surface are
 262 taken to be 552, 168 and 240 respectively. The time step is specified to be $T/100$. In order to
 263 reproduce the hydrodynamic properties of the OWC integrated system, the artificial and
 264 nonlinear pneumatic damping coefficients are chosen as $\mu_1 = 0.07$ and $\mu_2 = 1.65$, respectively.

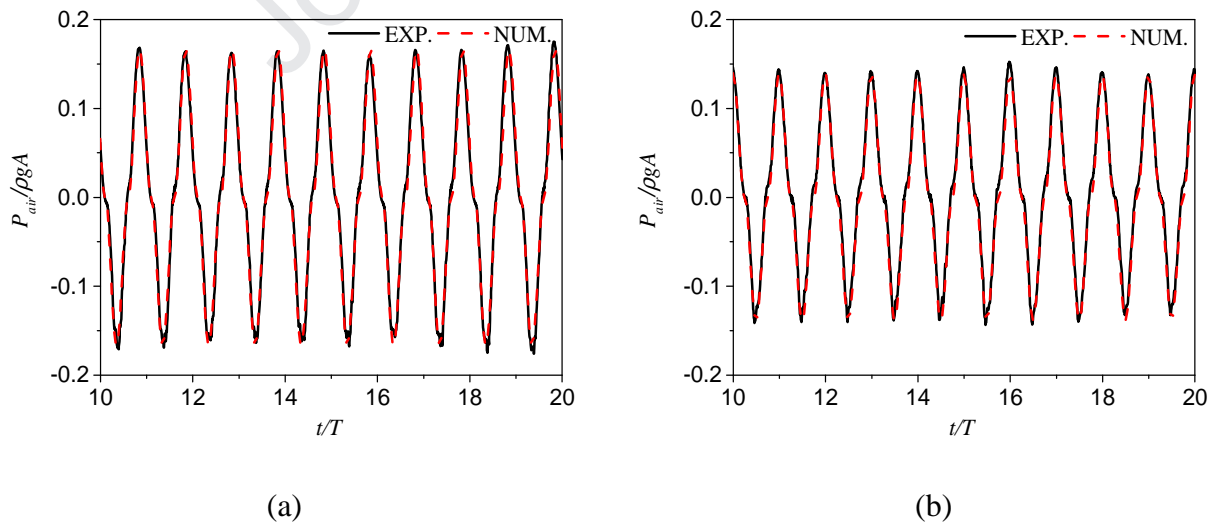
265 Fig. 6 and Fig. 7 show the time series of the surface elevation at G_3 and air pressure P_{air}
 266 in the chamber, respectively. Two dimensionless wave numbers, i.e. $kh = 1.99$ and 2.42 , are
 267 selected in the plots. It can be seen that the simulated and measured results agree well with
 268 each other. Both the free surface and air pressure can be observed the periodic variations over
 269 a long period. Fig. 8 presents the time history of the hydrodynamic pressures at different
 270 measuring points, as indicated in Fig. 3, at $kh = 1.99$. The superscript c denotes the
 271 corresponding results on the isolated OWT monopile. The predicted hydrodynamic pressures
 272 on the OWC shell and OWT monopile show good agreements with the experimental results. It
 273 should be noted that the experimental data at test point P_7 was not included in this study due
 274 to the accident fault of the proposed pressure sensor. From the figure, it is clear that relatively
 275 large pressure amplitudes occur at test points P_1 , P_4 , P_7 and P_{10} , which are close to the free
 276 surface. The same phenomenon was also reported in the experimental study of a land-based
 277 OWC device (Ning et al., 2016).

278 The averaged relative errors $\bar{\sigma} = \left| \overline{N_{w,exp}} - \overline{N_{w,num}} \right| / \overline{N_{w,exp}} \times 100\%$ between the predicted and
 279 measured chamber surface elevation, air pressure and point pressure are shown in Table 3 and
 280 Table 4, respectively. $\overline{N_w}$ denotes the peak value of both predicted and measured results.
 281 Due to the effect of vortex shedding induced by the OWC shell, the relative errors of the
 282 pressure are larger at the test points S_{10} , S_{11} and S_{12} than others. Overall, the numerical
 283 simulations are in a good agreement with the experiments for the test cases. Fig. 9 shows the
 284 variations of the crest amplitude of the surface elevation η_{crest} at G_3 , the air pressure ΔP_{air}
 285 ($\Delta P_{air} = [P(t)_{air\max} - P(t)_{air\min}] / 2$) and the hydrodynamic efficiency ζ with the dimensionless wave

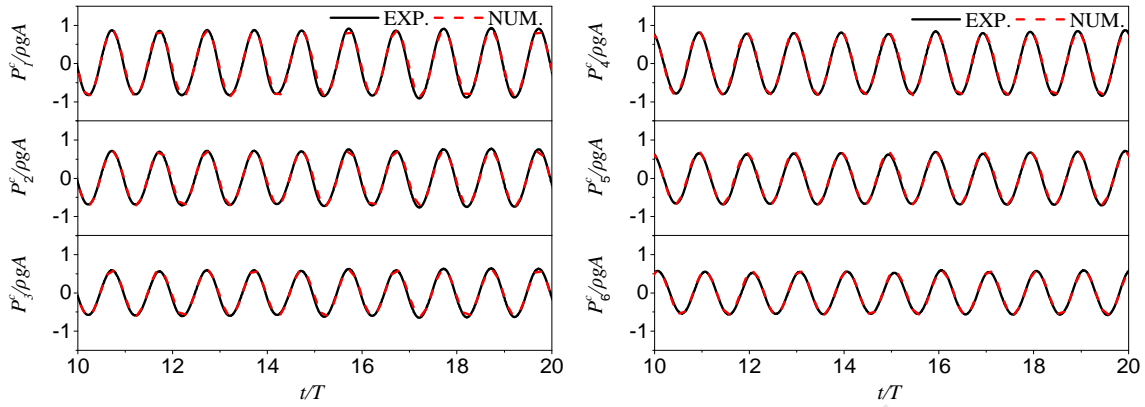
286 number kh . The wave frequency varies in the range of $1 \leq kh \leq 3$ with the same wave
 287 steepness $kA=0.05$. The results demonstrate that the amplitude of the surface elevation, the air
 288 pressure and the hydrodynamic efficiency exhibit similar variation with kh . The resonant
 289 frequency occurs at $kh=2.2$, which leads to a piston-type resonant phenomenon with
 290 maximum hydrodynamic efficiency of 52% and has ever been revealed in the previous
 291 theoretical research (Zhou et al., 2018). In summary, the present numerical results are all in
 292 close agreement with the experiments, verifying the suitability of the present HOBEM model.



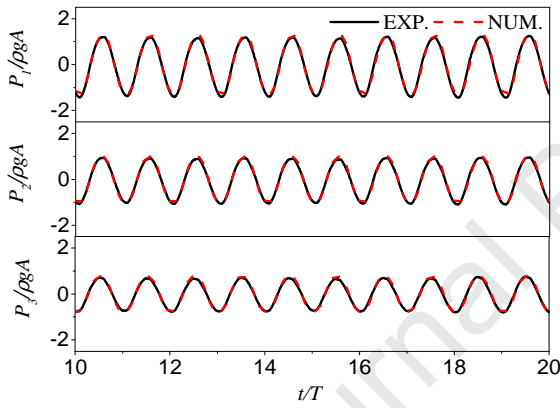
293
 294
 295 Fig. 6. Time series of the simulated and measured surface elevations at G_3 : (a) $kh=1.99$ and (b) $kh=2.42$.



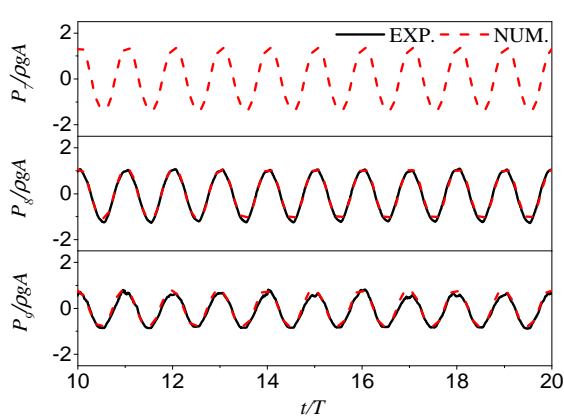
297
 298
 299 Fig. 7. Time series of the simulated and measured air pressure in the chamber: (a) $kh=1.99$ and (b) $kh=2.42$.



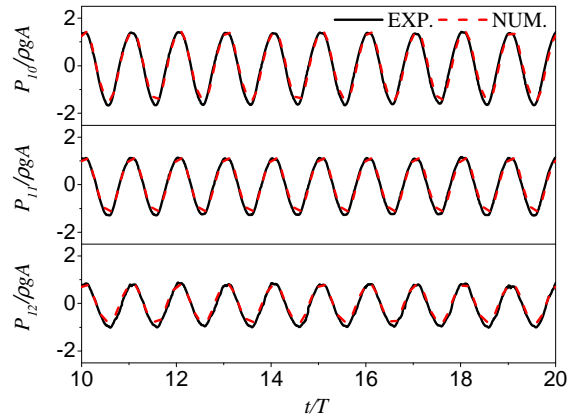
300

301 (a) At points S_1 , S_2 and S_3 without OWC shell(b) At points S_4 , S_5 and S_6 without OWC shell

302

303 (c) At points S_1 , S_2 and S_3 with OWC shell(d) At points S_4 , S_5 and S_6 with OWC shell

304

305 (e) At points S_7 , S_8 and S_9 306 (f) At points S_{10} , S_{11} and S_{12} Fig. 8. Comparisons of the simulated and measured pressures at different measuring points for $kh=1.99$.

307

308 Table 3 Averaged relative error between measured and predicted chamber surface elevation and air pressure

309

at the test points. (%)

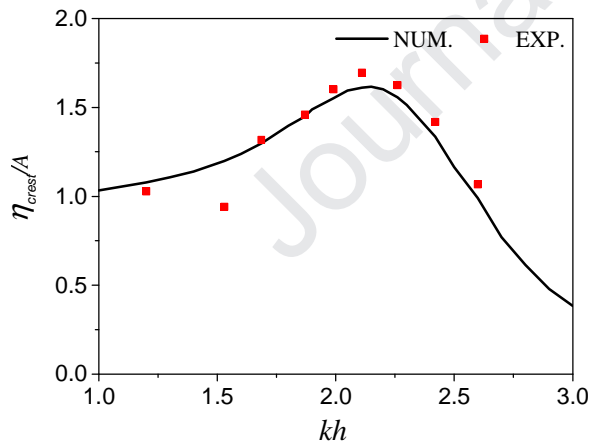
| Position | G_3 | \bar{S}_a |
|----------------------------|-------|-------------|
| $\bar{\sigma}_{(kh=1.99)}$ | 2.22 | 0.1 |
| $\bar{\sigma}_{(kh=2.42)}$ | 2.83 | 1.82 |

310

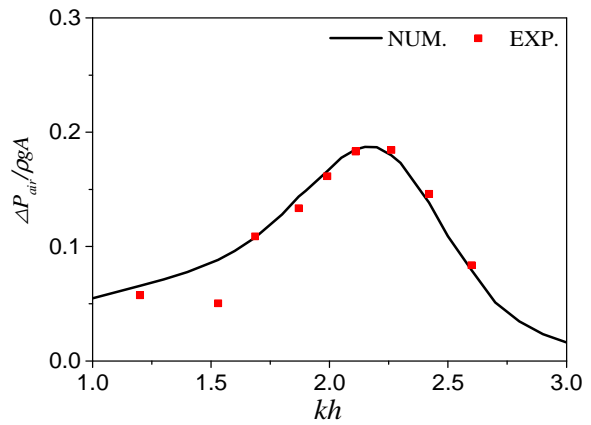
311 Table 4 Averaged relative error between measured and predicted pressure at the test points at $kh=1.99$. (%)

| Position | S ₁ | S ₂ | S ₃ | S ₄ | S ₅ | S ₆ | S ₈ | S ₉ | S ₁₀ | S ₁₁ | S ₁₂ |
|--|----------------|----------------|----------------|----------------|----------------|----------------|----------------|----------------|-----------------|-----------------|-----------------|
| $\bar{\sigma}_{(without\ OWC\ shell)}$ | 2.35 | 0.5 | 4.7 | 0.7 | 1.28 | 1.26 | | | | | |
| $\bar{\sigma}_{(with\ OWC\ shell)}$ | 1.78 | 1.27 | 6.7 | 1.19 | 5.69 | 4.0 | 7.13 | 0.1 | 10.9 | 5.61 | 5.63 |

312



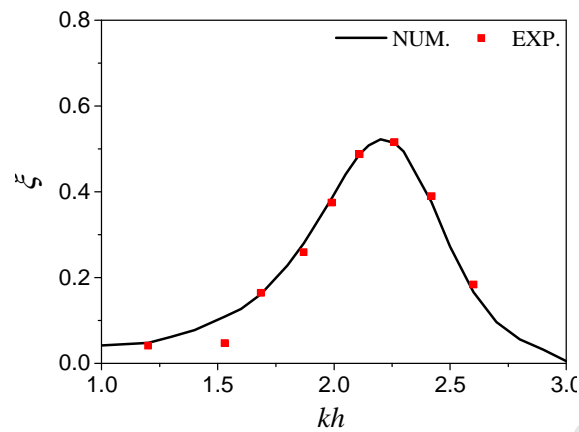
313

(a) surface elevation amplitude at G_3 

314

(b) chamber air pressure amplitude

315



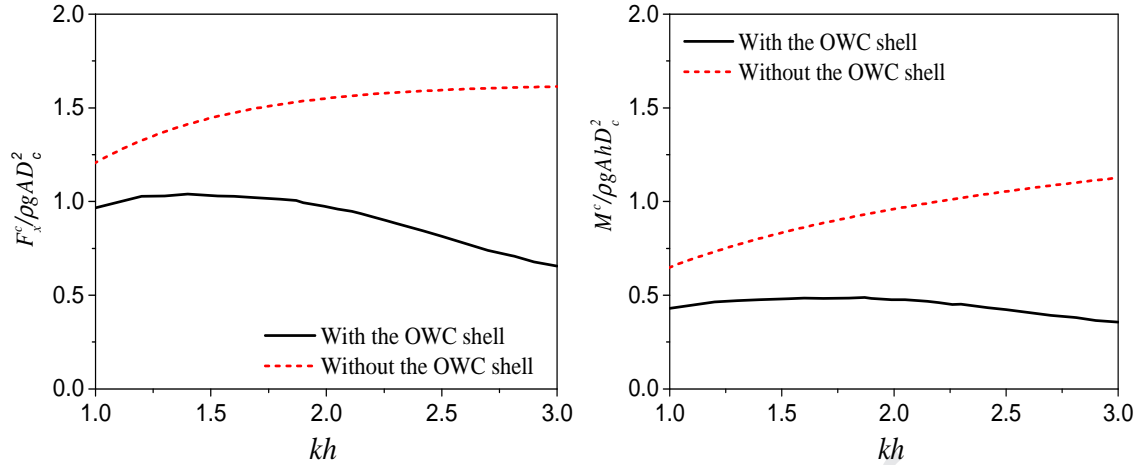
(c) hydrodynamic efficiency

Fig. 9. Distribution of the amplitudes of surface elevation and air pressure in the chamber and 5 hydrodynamic efficiency with the dimensionless wave number

3. Results and Discussions

3.1. Wave loads on the OWT monopile

In this section, the wave loads on the OWT monopile with different conditions are discussed. Fig. 10 illustrates the wave loads on the OWT monopile with and without the OWC chamber shell. The moment is about the rotational center point (0m, 0m, -1m). From the figure, it can be seen that the non-dimensional horizontal force $F_x/\rho gAD_c^2$ and overturning moment $M/\rho gAhD_c^2$ both significantly reduce with the introduction of the OWC shell, especially for the high-frequency waves. It is due to the OWC shell redistributes the wave potential around the OWT monopile to reduce the wave loads. Besides, the viscous drag and flow separation may also be generated around the thin OWC chamber, also contributing to the reduction of the wave loads. For short waves, they can be easily reflected by the large OWC shell, which leads to further reduction of wave loads on the OWT monopile in the high-frequency region.



(a) Horizontal force

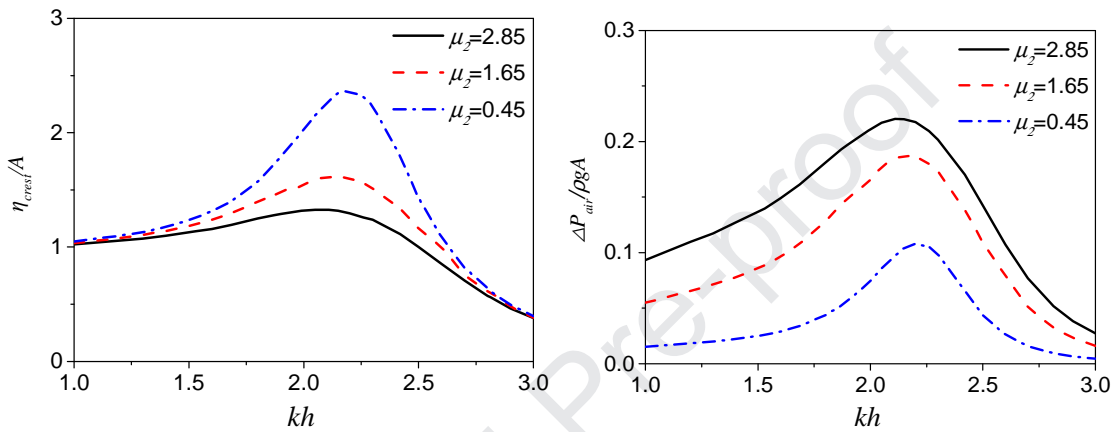
(b) Overturning moment

Fig. 10. Wave loads on the OWT monopile versus dimensionless wave number kh .

3.2. Effects of turbine damping

In order to investigate the influence of turbine damping on the hydrodynamic response of the OWC chamber, three different nonlinear pneumatic damping coefficients are considered, i.e., $\mu_2=0.45$, 1.65 and 2.85. The main geometric parameters of the OWC integrated system are set as $R_1=0.1\text{m}$, $R_2=0.4\text{m}$, $d=0.3\text{m}$, $d_c=0.2\text{m}$ and the wave steepness is kept to be $kA=0.05$. Fig. 11 demonstrates the influence of the turbine damping on the non-dimensional amplitudes of the surface elevation η/A at G_3 , the air pressure $\Delta P_{air}/\rho g A$ and the hydrodynamic efficiency ζ . From the figure, it can be seen that the PTO damping has a significant influence on both the surface elevation η and air pressure ΔP_{air} at the resonant frequency ($kh=2.2$). Such a behaviour has also been found in a small-scale experimental study of a floating cylindrical OWC device (Sheng et al., 2012). The air pressure increases and the surface elevation decrease with the pneumatic coefficient μ_2 increasing. From Fig. 11(c), it can be concluded that the maximal hydrodynamic efficiency is achieved at the resonant frequency regardless of the value of the pneumatic coefficient μ_2 , which is varied from 0.45 to 2.85 in this study. It can be apparently seen that the effective frequency bandwidth broadens with the increase of the pneumatic coefficient μ_2 , which benefits the power generation in the irregular

354 wave state. Besides, the dimensionless surface elevation amplitude is close to unity in
 355 the low-frequency region in Fig.11(a), which means that the effect of long wave is more
 356 apparent than the turbine damping (Zhou et al., 2018). And the air pressure ΔP_{air}
 357 increases as the coefficient μ_2 increases in the low-frequency region. Therefore, it is
 358 possible to enhance the hydrodynamic efficiency in the low-frequency region by raising
 359 the turbine damping.

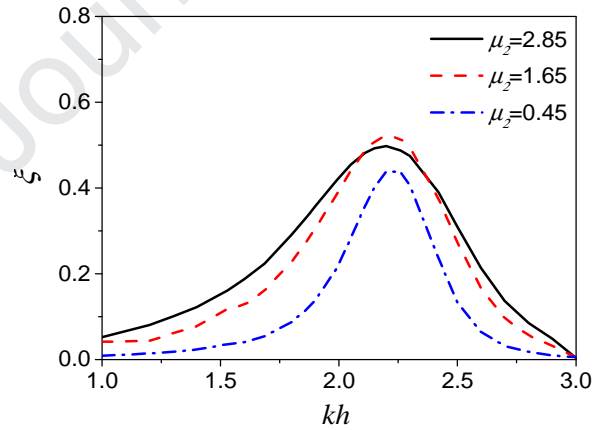


360

361

(a) Amplitude of the surface elevation at G_3

(b) Amplitude of the chamber air pressure



362

363

(c) Hydrodynamic efficiency

364

Fig. 11. Effects of the turbine damping on the hydrodynamic properties of the OWC chamber.

365

366

367

The wave dynamics on the OWT monopile is further investigated. Fig. 12 displays the variation of pressure at the points S_1 and S_4 with the pneumatic coefficient μ_2 . The

368 curve of pressure amplitude versus kh shows a similar trend to that of the surface
 369 elevation in Fig. 11(a). The resonant frequency also occurs at $kh=2.2$. It can be concluded
 370 that the pressure on the device is correlated with the free-surface motion in the chamber.
 371 The OWC system with larger turbine damping can reduce the local pressure on both the
 372 OWC shell and monopile. To further illustrate the pressure distribution on the OWT
 373 monopile, Fig. 13 shows the effects of the turbine damping on the non-dimensional
 374 pressure distribution $\Delta P/\rho g A$ along the seaside of the OWT monopile at resonant
 375 frequency ($kh=2.2$). It is clear that a huge pressure drops (at least 65%) occur under the
 376 relative water depth $z/h=0.4$. It illustrates that the wave energy is mainly concentrated on
 377 the fluid domain nearby the free surface. From Fig 13, it can be seen that the drop rate of
 378 the pressure increases with the decrease of the turbine damping μ_2 at the resonant
 379 frequency. This is due to the increase of the chamber surface elevation, which is greatly
 380 connected with the turbine damping μ_2 shown in Fig 11(a).

381

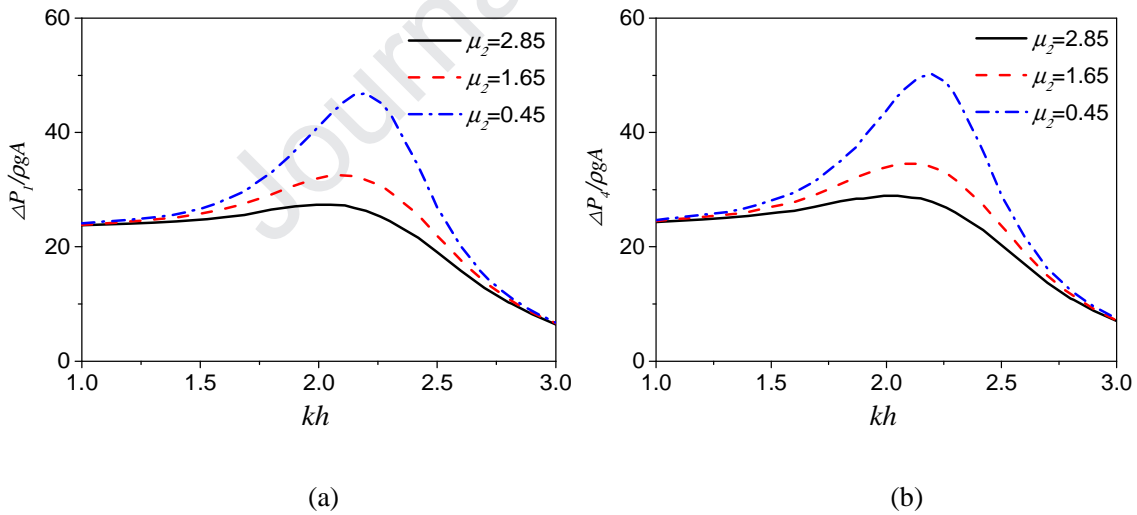
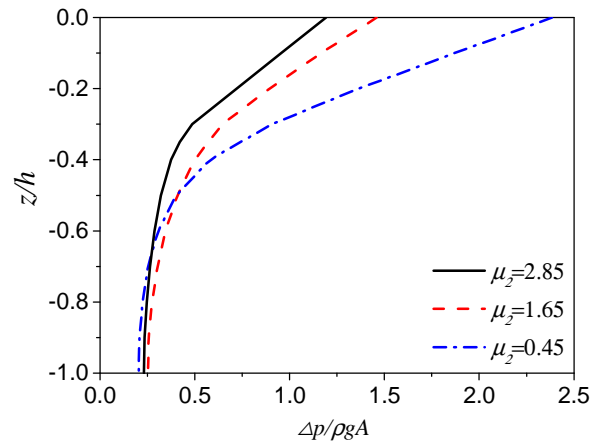


Fig. 12. Effects of the turbine damping on the pressures of test points (a) P_1 and (b) P_4 .



385

386 Fig. 13. Effects of the turbine damping on the pressure distribution along the seaside of the OWT monopile.

387

388 3.3. Effects of wave steepness

389

390

391

392

393

394

395

396

397

398

399

400

401

402

403

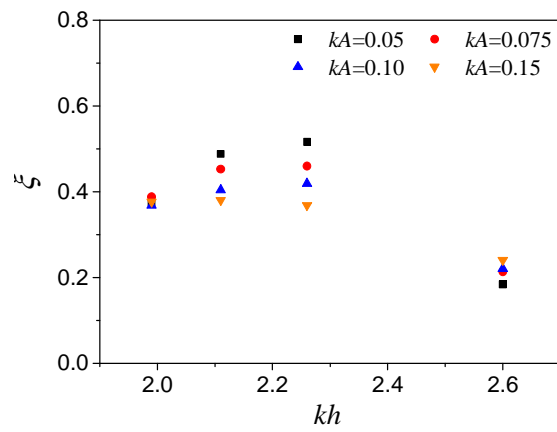
404

405

In this section, the nonlinear effects on the hydrodynamic performance of the OWC chamber are experimentally investigated under different wave steepness. The experiments are considered with four different wave steepness ($ka=0.05, 0.075, 0.10$ and 0.15) and four different wave conditions ($kh=2.6, 2.26, 2.11$ and 1.99), as shown in Table 2. Fig. 14 shows the hydrodynamic efficiency of the OWC device versus the wave steepness ka . As the wave steepness ka increases, the hydrodynamic efficiency generally decreases, especially near the resonant frequency ($kh=2.2$). As the wave steepness ka increases from 0.05 to 0.15 , the hydrodynamic efficiency of the OWC device reduces by 16.6% at $kh=2.26$. The same phenomenon was ever found in the land-fixed OWC devices (López et al., 2015). The reason is due to higher harmonics with more energy transferred from the fundamental wave easily reflected by the chamber external shell in the case of stronger nonlinear waves.

To further illustrate the physics in detail, the non-dimensional amplitudes of the surface elevation η_{crest}/A at G_3 and the air pressure $\Delta P_{air}/\rho g A$ are presented in Fig. 15. The dimensionless surface elevation η_{crest}/A inside the chamber decreases greatly with the increase of wave steepness ka , especially in the resonant region. As ka increases from 0.05 to 0.15 , the dimensionless surface elevation η_{crest}/A reduces by 39.7% at

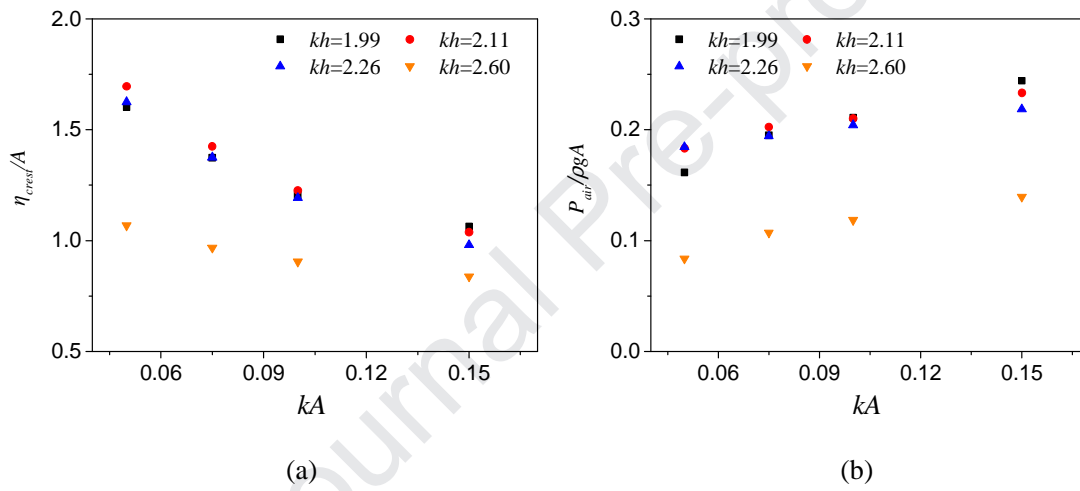
406 $kh=2.26$, which is larger than that (21.9%) at $kh=2.6$. It should be noted that η_{crest}/A
407 denotes a relative value normalized by the incoming wave amplitude. To further analyze
408 the nonlinear effects on the chamber free-surface-elevation, the results of the spectral
409 frequency analysis at the test point G_3 for different wave steepness kA are shown in Fig.
410 16. From the figure, it can be seen that fundamental and second-order waves occur in the
411 chamber, but the fundamental waves are the dominant. Furthermore, the dimensionless
412 amplitude of the fundamental wave decrease with the increase of the wave steepness kA .
413 It further illustrates the stronger reflection of the OWC chamber shell for the higher
414 harmonic waves, which lead to a smaller dimensionless surface elevation η_3/A . Fig. 15(b)
415 shows the variations of the dimensionless air pressure versus the wave steepness kA .
416 Compared with the dimensionless surface elevation amplitude in Fig. 15(a), the
417 dimensionless air pressure amplitude follows an opposite trend with the wave steepness
418 kA . Elhanafi and Chan (2018) also observed that the dimensionless air pressure increases
419 with the wave height over the entire frequency range. This result can be attributed to the
420 surface variation rate $(\eta_{max(t)}-\eta_{min(t)})/T$, which increases with the wave steepness kA and
421 thus the compression rate of the pneumatic air inside the OWC chamber increases. The
422 air pressure inside the chamber increases by 18.4% as kA increases from 0.05 to 0.15 at
423 $kh = 2.26$. However, the dimensionless surface elevation η_{crest}/A inside the chamber
424 decreases more at the same conditions, which leads to the decrease of the hydrodynamic
425 efficiency.
426



427

428

Fig. 14. Effects of the wave steepness kA on the hydrodynamic efficiency.



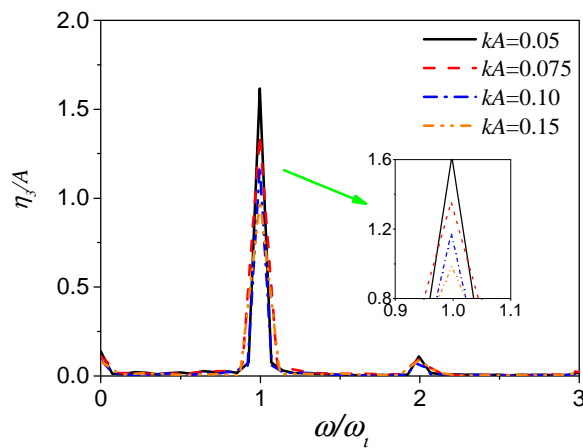
429

430

431

432

Fig. 15. Effects of the wave steepness kA on the (a) surface elevation η at G_3 and (b) chamber air pressure ΔP_{air} .



433

434

Fig. 16. Spectral frequency analysis of the chamber free surface elevation η_3 at $kh=2.26$.

435 **4. Conclusions**

436 In the present study, the hydrodynamic performance of an OWC wave energy converter
437 integrated into a fixed OWT monopile was investigated numerically and experimentally. The
438 OWC device is able to not only absorb the wave energy, but also reduce wave loads on the
439 OWT monopile. Based on linear potential flow theory, a 3D time-domain HOBEM model is
440 applied to simulate the OWC integrated system. The numerical results show good agreement
441 with the experimental data. The hydrodynamic performance of the OWC integrated system is
442 further investigated, especially the effects of the turbine damping and wave steepness.

443 The wave loads on the OWT monopile with or without the OWC chamber are discussed.
444 The OWC chamber shell can reduce the horizontal force and overturning moment on the
445 monopile. The PTO damping has a significant influence on the free surface elevation, the air
446 pressure in the chamber and the hydrodynamic efficiency. The wave steepness has a
447 significant influence on the hydrodynamic efficiency, especially near the resonant frequency.
448 An increase in the wave steepness results in a decrease of the nondimensional surface
449 elevation in the chamber and an increase of the chamber air pressure.

450 The present study neglects the effects of extreme waves, which often occur in the ocean.
451 In evaluating the reliability and viability of the device, the extreme wave load is a key
452 parameter. Therefore, future work will focus on the effects of irregular and extreme waves on
453 the complete system.

454

455 **Acknowledgements**

456 This work is supported by the National Key R&D Program of China (Grant No.
457 2018YFB151905), National Natural Science Foundation of China (Grant Nos. 51679036 and
458 51761135011) and EPSRC (Grant No. EP/R007519/1).

459

460

461 **References**

462 Achmus, M., Kuo, Y.S., Abdel-Rahman, K., 2009. Behavior of monopile foundations under
463 cyclic lateral load. *Computers and Geotechnics* 36, 725-735.

- 464 Aemesto, I., Guanche, R., Alvar, J.A.A., Alves, M.A., Vidal, C., Losada, I., 2014.
465 Time-domain modeling of a fixed detached oscillating water column towards a
466 floating multi-chamber device. *Ocean Eng.* 76, 65-74.
- 467 Bahaj, A.B.S., 2011. Generating electricity from the oceans. *Renewable Sustainable Energy*
468 *Reviews* 15, 3399-3416.
- 469 Bai, W., Teng, B., 2013. Simulation of second-order wave interaction with fixed and floating
470 structures in time domain. *Ocean Eng.* 74, 168-177.
- 471 Chen, L., Stagonas, D., Santo, H., Buldakov, E., Simons, R., Taylor, P., Zang, J., 2019.
472 Numerical modelling of interactions of waves and sheared currents with a surface
473 piercing vertical cylinder. *Coast. Eng.* 145, 65-83.
- 474 Cheng, Z., Wen, T.R., Ong, M.C., Wang, K., 2019. Power performance and dynamic
475 responses of a combined floating vertical axis wind turbine and wave energy converter
476 concept. *Energy* 171, 190-204.
- 477 da Fonseca, F.C., Gomes, R., Henriques, J., Gato, L., Falcao, A., 2016. Model testing of an
478 oscillating water column spar-buoy wave energy converter isolated and in array:
479 Motions and mooring forces. *Energy* 112, 1207-1218.
- 480 Elhanafi, A., Chan, J.K., 2018. Experimental and numerical investigation on wave height and
481 power take-off damping effects on the hydrodynamic performance of an
482 offshore-stationary OWC wave energy converter. *Renew. Energy* 125,
483 S0960148118302830.
- 484 Elhanafi, A., Macfarlane, G., Fleming, A., Zhi, L., 2017. Investigations on 3D effects and
485 correlation between wave height and lip submergence of an offshore stationary OWC
486 wave energy converter. *Appl. Ocean Res.* 64, 203-216.
- 487 Falcão, A.F., Henriques, J.C., Gato, L.M., Gomes, R.P., 2014. Air turbine choice and
488 optimization for floating oscillating-water-column wave energy converter. *Ocean Eng.*
489 75, 148-156.
- 490 Falcão, A.F.O., Henriques, J.C.C., 2016. Oscillating-water-column wave energy converters
491 and air turbines: A review. *Renew. Energy* 85, 1391-1424.
- 492 Ferrant, P., 1993. Threedimensional Unsteady Wave-Body Interactions by a Rankine
493 Boundary Element Method. *Ship Technology Research* 40, 165-175.
- 494 Gomes, R.P.F., Henriques, J.C.C., Gato, L.M.C., Falcão, A.F.O., 2016. Wave power extraction
495 of a heaving floating oscillating water column in a wave channel. *Renew. Energy* 99,
496 1262-1275.
- 497 Haji, M.N., Kluger, J.M., Sapsis, T.P., Slocum, A.H., 2018. A symbiotic approach to the
498 design of offshore wind turbines with other energy harvesting systems. *Ocean Eng.*
499 169, 673-681.
- 500 He, F., Leng, J., Zhao, X., 2017. An experimental investigation into the wave power
501 extraction of a floating box-type breakwater with dual pneumatic chambers. *Appl.*
502 *Ocean Res.* 67, 21-30.
- 503 He, F., Zhang, H., Zhao, J., Zheng, S., Iglesias, G., 2019. Hydrodynamic performance of a
504 pile-supported OWC breakwater: An analytical study. *Appl. Ocean Res.* 88, 326-340.
- 505 Heath, T.V., 2012. A review of oscillating water columns. *Philosophical Transactions of the*

- 506 Royal Society London 370, 235-245.
- 507 Jin, R., Teng, B., Ning, D., Zhao, M., Cheng, L., 2017. Numerical investigation of influence
508 of wave directionality on the water resonance at a narrow gap between two rectangular
509 barges. *Acta Oceanologica Sinica* 36, 104-111.
- 510 Kim, Y., 2003. Artificial Damping In Water Wave Problems I: Constant Damping. *Int. J.*
511 *Offshore Polar* 13.
- 512 Koo, W., Kim, M.H., 2010. Nonlinear Time-Domain Simulation of a Land-Based Oscillating
513 Water Column. *Journal of Waterway Port Coastal Ocean Engineering* 136, 276-285.
- 514 Liang, L., Yan, G., Yuan, Z., Day, S., Hu, Z., 2017. Dynamic response and power production
515 of a floating integrated wind, wave and tidal energy system. *Renew. Energy* 116,
516 S0960148117309217.
- 517 López, I., Pereiras, B., Castro, F., Iglesias, G., 2015. Performance of OWC wave energy
518 converters: influence of turbine damping and tidal variability. *International Journal of*
519 *Energy Research* 39, 472-483.
- 520 Mahnamfar, F., Altunkaynak, A., 2017. Comparison of numerical and experimental analyses
521 for optimizing the geometry of OWC systems. 130, 10-24.
- 522 Medina-Lopez, E., Ferrando, A.M., Gilabert, M.C., Pino, C.d., Rodríguez, M.L., 2016. Note
523 on a real gas model for OWC performance. *Renew. Energy* 85, 588-597.
- 524 Michailides, C., Gao, Z., Moan, T., 2016. Experimental study of the functionality of a
525 semisubmersible wind turbine combined with flap-type Wave Energy Converters.
526 *Renew. Energy* 93, 675-690.
- 527 Morris-Thomas, M.T., Irvin, R.J., Thiagarajan, K.P., 2007. An investigation into the
528 hydrodynamic efficiency of an oscillating water column. *Journal of Offshore*
529 *Mechanics and Arctic Engineering* 129, 273-278.
- 530 Ning, D.-z., Zhou, Y., Mayon, R., Johanning, L., 2020. Experimental investigation on the
531 hydrodynamic performance of a cylindrical dual-chamber Oscillating Water Column
532 device. *Appl. Energy* 260, 114252.
- 533 Ning, D., Zhou, Y., Zhang, C., 2018. Hydrodynamic modeling of a novel dual-chamber OWC
534 wave energy converter. *Appl. Ocean Res.* 78, 180-191.
- 535 Ning, D.Z., Shi, J., Zou, Q.P., Teng, B., 2015. Investigation of hydrodynamic performance of
536 an OWC (oscillating water column) wave energy device using a fully nonlinear
537 HOBEM (higher-order boundary element method). *Energy* 83, 177-188.
- 538 Ning, D.Z., Wang, R.Q., Chen, L.F., Sun, K., 2019. Experimental investigation of a
539 land-based dual-chamber OWC wave energy converter. *Renew. Sust. Energ. Rev.* 105,
540 48-60.
- 541 Ning, D.Z., Wang, R.Q., Ying, G., Ming, Z., Teng, B., 2016. Numerical and experimental
542 investigation of wave dynamics on a land-fixed OWC device. *Energy* 115, 326-337.
- 543 Ohlenforst, K., Council, G.W.E., 2019. *Global Wind Report 2018*. Recuperado.
- 544 Paulsen, B.T., Sonnevile, B.d., Meulen, M.v.d., Jacobsen, N.G., 2019. Probability of wave
545 slamming and the magnitude of slamming loads on offshore wind turbine foundations.
546 *Coast. Eng.* 143, 76-95.
- 547 Pechak, O., Mavrotas, G., Diakoulaki, D., 2011. Role and contribution of the clean

- 548 development mechanism to the development of wind energy. *Renewable Sustainable*
549 *Energy Reviews* 15, 3380-3387.
- 550 Perez-Collazo, C., Greaves, D., Iglesias, G., 2018. Hydrodynamic response of the WEC
551 sub-system of a novel hybrid wind-wave energy converter. *Energy Convers. Manage.*
552 171, 307-325.
- 553 Pérez-Collazo, C., Greaves, D., Iglesias, G., 2015. A review of combined wave and offshore
554 wind energy. *Renewable Sustainable Energy Reviews* 42, 141-153.
- 555 Perez-Collazo, C., Richard, P., Greaves, D., Iglesias, G., 2019. Monopile-mounted wave
556 energy converter for a hybrid wind-wave system. *Energy Convers. Manage.* 199,
557 111971.
- 558 Ren, N., Zhe, M., Fan, T., Zhai, G., Ou, J., 2018. Experimental and numerical study of
559 hydrodynamic responses of a new combined monopile wind turbine and a heave-type
560 wave energy converter under typical operational conditions. *Ocean Eng.* 159, 1-8.
- 561 Rezanejad, K., Bhattacharjee, J., Soares, C.G., 2013. Stepped sea bottom effects on the
562 efficiency of nearshore oscillating water column device. *Ocean Eng.* 70, 25-38.
- 563 Sarmiento, J., Iturrioz, A., Ayllón, V., Guanche, R., Losada, I.J., 2019. Experimental
564 modelling of a multi-use floating platform for wave and wind energy harvesting.
565 *Ocean Eng.* 173, 761-773.
- 566 Shalby, M., Elhanafi, A., Walker, P., Dorrell, D.G., 2019. CFD modelling of a small-scale
567 fixed multi-chamber OWC device. *Appl. Ocean Res.* 99, 37-47.
- 568 Sheng, W., 2019. Wave energy conversion and hydrodynamics modelling technologies: A
569 review. *Renew. Sust. Energ. Rev.* 109, 482-498.
- 570 Sheng, W., Alcorn, R., Lewis, A., 2013. On thermodynamics in the primary power conversion
571 of oscillating water column wave energy converters. *J. Renew. Sustain. Ener.* 5,
572 1257-1294.
- 573 Sheng, W., Flannery, B., Lewis, A., Alcorn, R., 2012. Experimental Studies of a Floating
574 Cylindrical OWC WEC. In: 31st International Conference on Ocean, Offshore and
575 Arctic Engineering, ASME 169-178. in Rio de Janeiro, Brazil.
- 576 Simonetti, I., Cappietti, L., Elsafti, H., Oumeraci, H., 2017. Optimization of the geometry and
577 the turbine induced damping for fixed detached and asymmetric OWC devices: A
578 numerical study. 139, 1197-1209.
- 579 Slot, R.M., Sørensen, J.D., Sudret, B., Svenningsen, L., Thøgersen, M.L., 2019. Surrogate
580 model uncertainty in wind turbine reliability assessment. *Renew. Energy.*
- 581 Soares, C.G., 1995. Offshore structure modelling. World Scientific.
- 582 Wan, L., Gao, Z., Moan, T., 2015. Experimental and numerical study of hydrodynamic
583 responses of a combined wind and wave energy converter concept in survival modes.
584 *Coast. Eng.* 104, 151-169.
- 585 Wang, R.Q., Ning, D.Z., Zhang, C.W., Zou, Q.P., Liu, Z., 2018. Nonlinear and viscous effects
586 on the hydrodynamic performance of a fixed OWC wave energy converter. *Coast. Eng.*
587 131, 42-50.
- 588 Wind-Europe, Wind Europe, 2019. Offshore Wind in Europe: Key Trends and Statistics 2018.
589 Brussels, Belgium.

- 590 Wu, X., Hu, Y., Li, Y., Yang, J., Liao, S., 2019. Foundations of offshore wind turbines: A
591 review. *Renewable Sustainable Energy Reviews* 104, 379-393.
- 592 Xu, C., Huang, Z., Deng, Z., 2016. Experimental and theoretical study of a cylindrical
593 oscillating water column device with a quadratic power take-off model. *Appl. Ocean*
594 *Res.* 57, 19-29.
- 595 Zheng, S., Antonini, A., Zhang, Y., Greaves, D., Miles, J., Iglesias, G., 2019. Wave power
596 extraction from multiple oscillating water columns along a straight coast. *J. Fluid*
597 *Mech.* 878, 445-480.
- 598 Zheng, S., Zhang, Y., Iglesias, G., 2018. Wave–structure interaction in hybrid wave farms. *J.*
599 *Fluid. Struct.* 83, 386-412.
- 600 Zhou, Y., Zhang, C., Ning, D., 2018. Hydrodynamic Investigation of a Concentric Cylindrical
601 OWC Wave Energy Converter. *Energies* 11, 985.
- 602

Highlights:

1. An OWC and OWT integrating system was proposed.
2. A quadratic PTO model predicts the OWC chamber hydrodynamic performance well.
3. The OWC shell can effectively reduce the wave loads on the OWT monopile.
4. The hydrodynamic efficiency of the OWC device decreases with the wave nonlinearity.

Journal Pre-proof

Declaration of interests

The authors declare that they have no known competing financial interests or personal relationships that could have appeared to influence the work reported in this paper.

The authors declare the following financial interests/personal relationships which may be considered as potential competing interests: